INTERNATIONAL JOURNAL OF HYDROGEN ENERGY 45 (2020) 7788–7800

Available online at www.sciencedirect.com

ScienceDirect

journal homepage: www.elsevier.com/locate/he

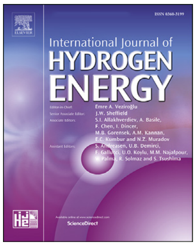

Improving hydrogen evolution reaction and capacitive properties on CoS/MoS$_2$ decorated carbon fibers

D.N. Sangeetha [a], D. Krishna Bhat [b], S. Senthil Kumar [c], M. Selvakumar [a,*]

[a] Department of Chemistry, Manipal Institute of Technology, Manipal Academy of Higher Education, Manipal, 576104, Karnataka, India
[b] Department of Chemistry, National Institute of Technology Karnataka, Surathkal, 575025, Karnataka, India
[c] Electrodics and Electrocatalysis Division, CSIR-Central Electrochemical Research Institute, Karaikudi, 630006, Tamil Nadu, India

HIGHLIGHTS

- High surface area carbon fibers synthesized from banana fibers.
- Nano CoS/MoS$_2$ grown on ACFs for enhanced supercapacitor and hydrogen evolution.
- High capacitance of 733 Fg-1 at 0.5 Ag^{-1} obtained for symmetric combination.
- Tafel slope of 61 mVdec^{-1} found for the ACFs/CoS/MoS$_2$ composite.

ARTICLE INFO

Article history:
Received 23 May 2019
Received in revised form
24 September 2019
Accepted 3 October 2019
Available online 31 October 2019

Keywords:
Pseudocapacitance
Specific capacitance
Power density
Tafel slope
Overpotential

ABSTRACT

We report a facile method to transform abundantly dumped banana stem fibers into carbon fibers (CFs) useful for energy applications. The CFs surface area is increased by varying the quantity of KOH activation to 488 m^{2}g^{-1}. The solvothermal method is used to synthesize CoS, CoS/MoS$_2$ and also grown on the activated carbon fibers (ACFs). Nano nodules of CoS arranged into sheets and layers of MoS$_2$ stacked together were found in FESEM analysis. The morphology of the CoS/MoS$_2$ differs when grown on ACFs. The growth of CoS/MoS$_2$ along the ACFs length prevents any stacking of the pseudocapacitance materials. The ternary composite ACFs/CoS/MoS$_2$ exhibits superior supercapacitor behavior as well as hydrogen evolution reaction (HER) due to the synergetic effect of the conducting ACF surface and redox active CoS/MoS$_2$. A maximum specific capacitance of 733 Fg^{-1}, energy and power density of 33 WhKg^{-1} and 999 WKg^{-1} respectively are obtained. A low Tafel slope value of 61 mVdec^{-1} is obtained for the ACFs/CoS/MoS$_2$ ternary composite electrode. The present work therefore offers a fresh insight into the effective conversion of waste materials into electrode material for energy storage and conversion applications.

---

* Corresponding author.
E-mail address: chemselva78@gmail.com (M. Selvakumar).

https://doi.org/10.1016/j.ijhydene.2019.10.033

Introduction

Carbon material has distinctive characteristics that make it usable in electroanalytical chemistry as electrodes. Due to the wide operating potential, relatively low cost, easy processability and chemical inertness in most of the electrolytes, porous carbons (one of the forms of carbon) have been mostly used as an active electric double layer capacitor (EDLC) electrode materials in recent years [1,2]. The incredible advancement of nanotechnology in material science, especially in the field of carbon nanofibers (CNFs), led its way to electrocatalysis. Discovery of Carbon nanofibers (CNFs) dates to 1889, centuries ago. A patent filed then mentioned the growth of carbon filaments on the metallic crucible on carbon-containing gasses passing through [3,4]. This material's properties were unknown and was therefore called carbon filaments. Robertson was the first person to understand and privy about these catalytic conversions [5]. He discovered graphic carbon formation at comparatively reduced temperatures owing to the interaction of methane and a metal. However, only recently did the proper use of these come to the fore. Carbon fibers (CFs) are lightweight carbon with a large specific surface area (SSA), 3–100 nm in diameter, 0.1–1000 μm in length, and have chemical similarities with fullerenes and carbon nanotubes. Their structure varies primarily in terms of graphene sheet stacking arrangements. The surface area relies on the graphitic or edge plane [6]. CFs ' 1-D architecture allows excellent access to electrolytes as well as provide longitudinally higher electronic conductivity. As per the early studies, the electrical resistance was found to be the lowest along the length direction of the CFs [7]. CFs are often used as supporting materials in terms of catalytic reaction. The CF's internal and external surfaces are chemically active in a catalytic reaction. In the case of HER also, CFs act as catalyst support materials [8,9]. CFs synthesis uses primarily organic compounds that are indirectly associated with fossil fuels. With growing concerns about depleting fossil fuels, rising pollution, and elevated price of CF precursors, an alternative for CF precursors is very much needed. Abundantly available biowastes present an opportunity. Bio precursors are still being regarded among several precursor materials for CF synthesis. By removing the lignin and maintaining cellulose as a carbon precursor, disposable bamboo chopsticks were transformed into carbon fibers. This carbon fiber material reported by J. Jiang et al. was utilized to fabricate Li-ion batteries. In order to synthesize highly ordered mesoporous carbon nanofibril arrays, Hai-Jing Liu used the naturally available templates such as the crab shell to provide a large SSA of 1270 m^2g^{-1} [10]. J. Xue et al. used cotton as the precursor to fabricate a supercapacitor (SCs) device, with response time as low as 50 ms [11]. Wood shavings were transformed to activated carbon fibers of 3223 m^2g^{-1} SSA and a specific capacity of up to 280 Fg^{-1} at 0.5 Ag^{-1} using 1 M H_2SO_4 [12]. Walnut shells were also used as the carbon precursor for the synthesis of CNFs with an average diameter of ~287 nm [13].

In order to attain effective electrochemical performance along with the large SSA of the carbon, electrochemically active surface should be considered [14]. The 2-dimensional morphology of pseudocapacitive inorganic materials would actively contribute to the distinctive physicochemical characteristics of SCs and HER. The Cobalt family (compounds such as CoS, CoSx, CoOx, CoS_2 and their composites) is one of the pseudocapacitive materials. These have been widely researched in recent decades as a pseudocapacitor electrode after electrocatalysts. A biomolecule, L-cysteine, was used to synthesize nanostructures of CoS as the Sulfur precursor. On testing CoS nanowires, a high specific capacitance of 508 Fg^{-1} was obtained at 2.5 $mAcm^{-2}$ [15]. The CoS can be grown along the length of CFs in order to achieve higher material performance without any agglomeration of these electroactive catalysts. One such example pertaining to such case for better performance is the three-dimensional graphene/CoS_x. This system delivered specific capacitance of 443 Fg^{-1} at 1 Ag^{-1}. The value is much higher than the single component system. By the end of 5000 cycles, 86% of the initial capacity was retained [16]. Moreover, the composite also provided a better evolution of hydrogen with a reduced Tafel slope of 93 $mVdec^{-1}$. When checked for water splitting in acidic medium, CoS nanosheets grew vertically on carbon cloth, yielded a reduced Tafel slope and overpotentials, maintaining excellent stability over 50 h [17].

The present research shows the use of the fibril framework in bananas pseudostems for CF synthesis, considering the above-mentioned opportunities. The availability of tons of discarded banana stems after harvest makes it affordable to use it effectively as electrode material for energy storage and conversion purposes. CoS and CoS/MoS_2 were grown on the synthesized CFs by solvothermal technique. The CFs and the composites (CF/CoS and CF/CoS/MoS_2) were subsequently tested for supercapacitor (SC) and hydrogen evolution reaction.

Materials and methods

Materials

Potassium Hydroxide (KOH) was procured from Finer reagents. Ammonium Molybdate Tetrahydrate was got from Spectrochem Pvt. Ltd. Sodium Sulphate (Na_2SO_4), and thiourea from Loba Chemie Pvt. Ltd., Sulphuric Acid (H_2SO_4), Nitric Acid (HNO_3) and Hydrochloric acid (HCl) were procured from Merck Specialties Pvt. Ltd.

Synthesis of carbon nanofibers and activation

The banana pseudostems were cut into horizontal pieces. The fiber was separated and dried in a hot air oven. The fibers were carbonized for an hour at 300 °C under N_2 atmosphere. The black powder obtained is carbon fiber. To improve the SSA, CF was activated. Different weight ratios of carbon fiber and KOH (1:3, 1:4, 1:5, 1:6, 1:7 and 1:8) were subjected to sonication for 12 h. The mixture was dried in an air oven and later activated for 1 h at 500 °C under N_2 atmosphere. The activated powder was first washed with 4 M HCl and then with plenty of water until the pH was neutral, in order to remove the dissolved salts. The precipitate obtained is then dried overnight in an air oven. The black powder obtained is termed as activated carbon nanofiber (ACFs).

Growth of CoS_2 on ACFs - termed as binary composite

2 mM cobalt acetate was mixed with 100 mM thiourea in 100 mL water and stirred for 2 h. It was allowed to settle for one day. The mixture was loaded in a 50 mL Teflon lined stainless steel autoclave and kept in the oven for 16 h at 180 °C. The precipitate was washed using excess water and ethanol. Dried overnight in an air oven.

CoS was grown on ACFs by following the above procedure. 0.5 g of ACFs was added and stirred along with the cobalt acetate- thiourea mixture in 100 mL of water. The mixture is treated as same as the above-mentioned procedure. The precipitate is termed as ACFs/CoS.

Synthesis of ACFs/CoS/MoS_2

2 mM cobalt acetate, 0.5 mM ammonium molybdate was mixed in 100 mL water containing 100 mM thiourea, stirred for 2 h and allowed to stand for a day. It was then loaded into a 50 mL Teflon lined stainless steel autoclave and placed in an oven maintained at 180 °C for 16 h. The obtained precipitate was washed with surplus water, then with ethanol, and dried overnight.

Following the above method of synthesis, CoS/MoS_2 was grown on ACFs. 0.5 g of ACFs was added to the mixture of 2 mM cobalt acetate, 0.5 mM ammonium molybdate, 100 mM thiourea mixture in 100 mL water. Hydrothermally treated at 180 °C for 16 h. The precipitate was collected, washed with water and ethanol. Dried overnight. The product is ACFs/CoS/MoS_2.

Material characterization

Nitrogen sorption analysis was carried out using Belsorp MR6, MicrotracBEL Corp., at 77 K using Brunauer, Emmett Teller (BET) calculations for SSA. Using the Bruker Miniflex 600 model, X-ray diffraction patterns were obtained within the range of 10º to 80º. X-ray photoelectron spectroscopy (XPS) spectra were recorded with Thermo Scientific MULTILAB 2000 using Mg Kα (1253.6 eV) exciting X-ray source. Laser Raman microscope was used to study the chemical nature of ACFs. Field-emission scanning electron microscopy equipped with energy dispersion X-ray (EDX) spectroscopy of ZEISS Sigma VP FE-SEM with Oxford EDS Sputtering System has been used to study morphology and elemental composition of the materials. High-resolution TEM images were obtained with Tecnai G2, F30 instrument at an acceleration voltage of 300 kV.

Electrochemical characterization

All electrochemical measurements were performed using Biologic SP 150 in 1 M Na_2SO_4 for supercapacitor assessment. The supercapacitor working electrode was fabricated as below. 80 wt % of synthesized materials (ACFs, CoS, ACFs/CoS, CoS/MoS_2 and ACFs/CoS/MoS_2), 10 wt % of acetylene black and 3–4 drops of the binder (PVDF and NMP) were mixed thoroughly to form a thick slurry. The slurry was then coated onto stainless steel (SS) current collector of 1 cm × 1 cm dimensions. This act as working electrode. Material mass of 2–5 mg/cm^2 was maintained on the SS. The polypropylene was used as a separator between the cathode and the anode in the case of symmetric SCs (SSC) and hybrid SCs (HSC). All the formulae for specific capacitance, energy density, power density, efficiency and time constant were followed from our previous work [18,19].

The electrode materials (ACFs, CoS, ACFs/CoS, CoS/MoS_2 and ACFs/CoS/MoS_2) were drop casted on the glass carbon for HER analysis. 20 mg of electrode material was well dispersed in a mixture of 50 μL Nafion in 250 μL water for 1 h. A sample of 10 μL is then drop cast onto the glassy carbon electrode. The HER analysis was carried out in N_2 purged 0.5 M H_2SO_4.

Results and discussions

Material characterization of the ACFs

The BET surface area measurement gave an SSA of 448 m^{2}g^{-1} with an average pore diameter of 0.70 nm and an average pore volume of 0.173 cm^{3}g^{-1}. Typically, the isotherm of adsorption-desorption was found to be the Ia-isotherm with narrower pore size distribution [20]. The results given in Fig. 1a are in good agreement with the isotherm reported by M. Thommes et al. The pore size distribution plot of ACFs is shown in Fig. 1b and c. The pore size recorded in this study is in the region of the narrow pore size representing the micropores. The carbonized fibers of banana pseudostems lack good specific surface area. In the beginning the surface area of the CFs was found to be 21 m^{2}g^{-1}. To enhance the CF's SSA, different activating agents were treated, varying different reaction parameters. Using hydrothermal method, NaOH was used to remove lignin from the stems. Then the material treated with NaOH was subjected to carbonization. However, it was found that the SSA achieved was only 12 m^{2}g^{-1}. NaOH was substituted with KOH and the same hydrothermal method was carried out. By doing so the SSA was enhanced, but not to the expected value. The resulting SSA was 63 m^{2}g^{-1}. Therefore, the method of KOH activation of pre-carbonized CFs was selected. The findings were much better than the two techniques described above. Hence, the more accessible method was fibral extract carbonization, followed by KOH activation. Studies show that pores induced by activation enhanced CF SSA, producing activated carbon fibers [21–24]. Thus, in the present case the SSA of the carbon fibers was enhanced through KOH activation technique. Activation was performed with different ratios of CF: KOH (1:3,1:4, 1:5, 1:6, 1:7 and 1:8) to obtain higher surface area. Among these, 1:5 ratio of the CFs: KOH produced a maximum SSA compared to the rest. The stacked layers of CFs are separated when KOH is added to the CF in water, sonicated and activated to 500 °C. The metallic potassium is generated at 500 °C (reaction 1) and begins to intercalate the stacked CF layers.

$$6KOH + 2C \rightarrow 2K + 3H_2 + 2K_2CO_3 \quad (1)$$

Carbon fibers undergo gasification because of the KOH products produced during activation. After intercalation, there is a local broadening of the CFs forming ladder like

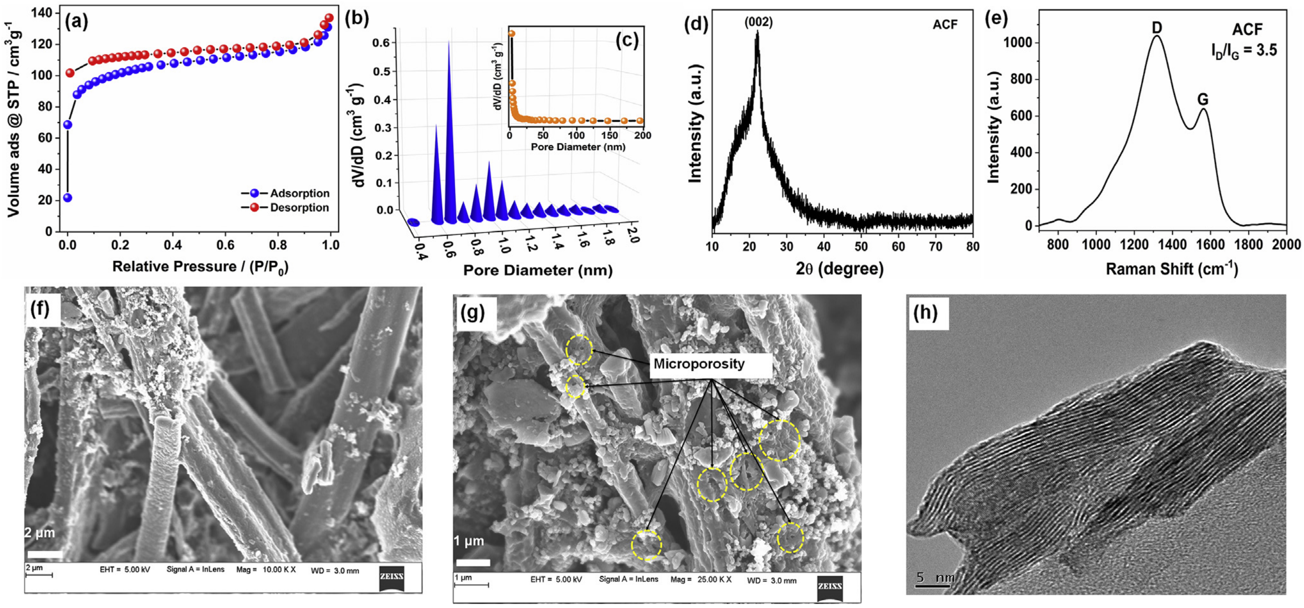

Fig. 1 – **(a) N_2 adsorption-desorption isotherm; (b) and (c) pore size distribution plots; (d) XRD; (e) Raman spectra; (f) SEM; (g) FESEM; (h) HRTEM of ACFs.**

structures of CFs. At constant temperature for an hour, these sheets collapse and finally rearrange graphene sheets of CFs. Thereby producing more exposed fibral carbon, or in other terms, enhancing the SSA of the CF after activation to produce ACFs. Fig. 1d is the XRD traces if the synthesized ACFs. The broad (002) peak indicates the existence of small graphitic domains present among the predominantly disordered carbon. However, the total degree of graphitization is minimal. The d_{002} spacings between the layers of ACFs, calculated using Bragg's law, was 0.56 nm.

Carbon fibers are typically defined in Raman spectra by two main peaks, the D and the G peaks (Fig. 1e.). The G mode resulting from the first order scattering of the E_{2g} photon of sp^2 C atoms and due to the in-phase vibration of graphite lattice. While the D mode arise from a breathing mode of j-point photons of A_{1g} symmetry [25]. FT-Raman spectra of the synthesized ACFs also show these two peaks at 1336 and 1574 cm^{-1} corresponding to carbon D and G peaks respectively. The D band's intensity is observed to be stronger than the intensity of the G band. The I_D/I_G ratio is used to correlate the structural purity of graphitic materials to the graphite crystal domain size, as obtained by X-ray diffraction. The intensity of the D band is considered to be dependent on defects. Greater the number of defects the greater would be the intensity of the D band. The obtained ratio was 3.5. The higher ratio is due to the defects or disorder in the crystalline surface structure, which is also apparent from the wide XRD pattern. In lignin-based carbon fibers, a low level of graphitic development is observed as inferred from large I_D/I_G ratio [26,27]. The I_D/I_G area ratio of lignin-derived carbon fibres has been reported in prior literatures studies to be 2–5 [28,29].

FESEM confirms the fibral morphology of the ACFs (Fig. 1f and g). In addition, the tubular structure does not have a hollow core, but a layered sheet stacked in one-dimension to produce the structure of the fibril. This layered stacking is clearly visible in HR-TEM image shown in Fig. 1h. In evidence to FE-SEM, the core of the ACFs is observed to be not hollow but several sheets seen to be stacked over to form a few layers in the fibril ACFs.

Material characterization of CoS and ACFs/CoS

The CoS XRD pattern is indexed to (100), (101), (102), (110) and (201) planes of the hexagonal phase (JCPDS – 65-3418). No other diffraction peaks were found, which infers the purity phase (Fig. 2a). Furthermore, in order to check the CoS deposition on ACFs, XRD of the ACFs/CoS was taken (Fig. 3a). A small broad peak was observed at 24°, corresponding to the graphitic (002) plane of the ACFs. Calculated from Scherer formula, the average crystallite size for CoS and ACFs/CoS was found to be 123 and 109 nm respectively. CoS and ACFs/CoS morphology was determined using FESEM shown in Fig. 2b, c of CoS and 3b, c for ACFs/CoS. On careful examination of the structure of CoS, it appears to be smaller node of CoS. These nodes grow in height and length to produce sheet. These sheets grow into flower shapes that resembles the cockscomb flower. Additionally, if we carefully examine the morphology of the ACFs/CoS, the CoS is seen wrapped up to the ACFs. The CoS nodes tend to develop along the length of the ACFs, hence the wrapping around them. These node like structure, however, was found to be in a few sheet forms of CoS wrapped along the length of ACFs which is evident from the HR-TEM images shown in Fig. 3d. If we notice the HR-TEM images of CoS (Fig. 2d, e, f), the edges of. these sheets were found to be wrapped up by several sheets as shown in Fig. 2f. Further, the composite on careful examination shows the growth of CoS on the fibril ACFs structures. The EDAX results are given in

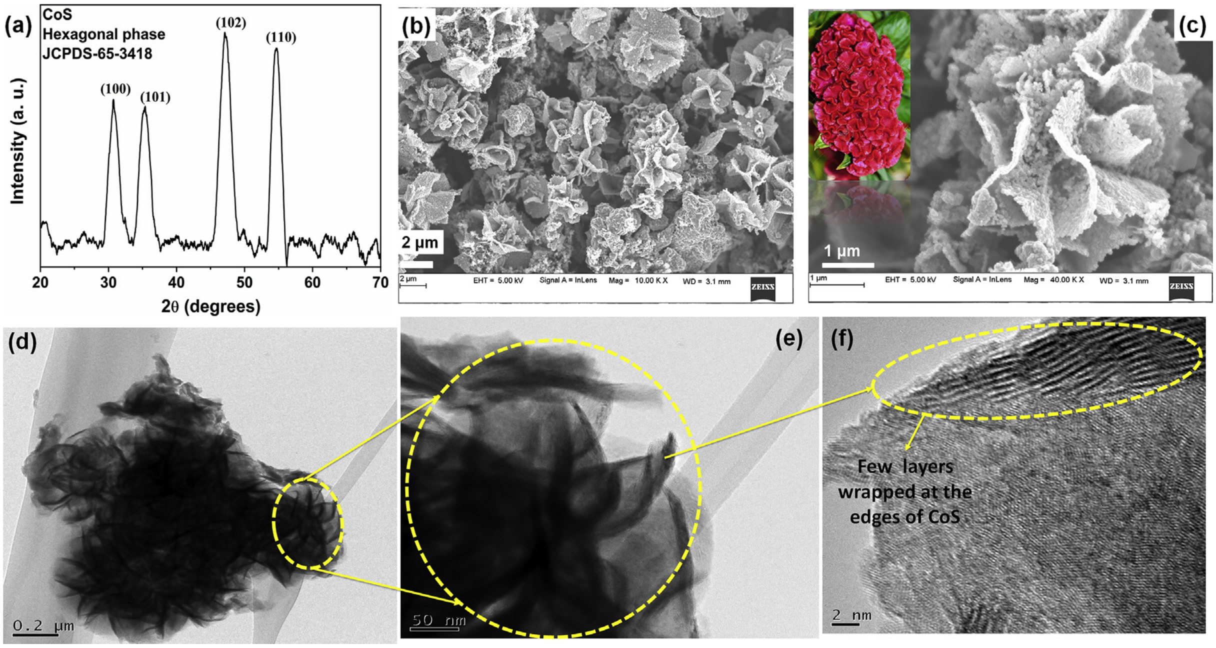

Fig. 2 – (a) XRD; (b) and (c) FESEM; (d)–(f) HRTEM of CoS.

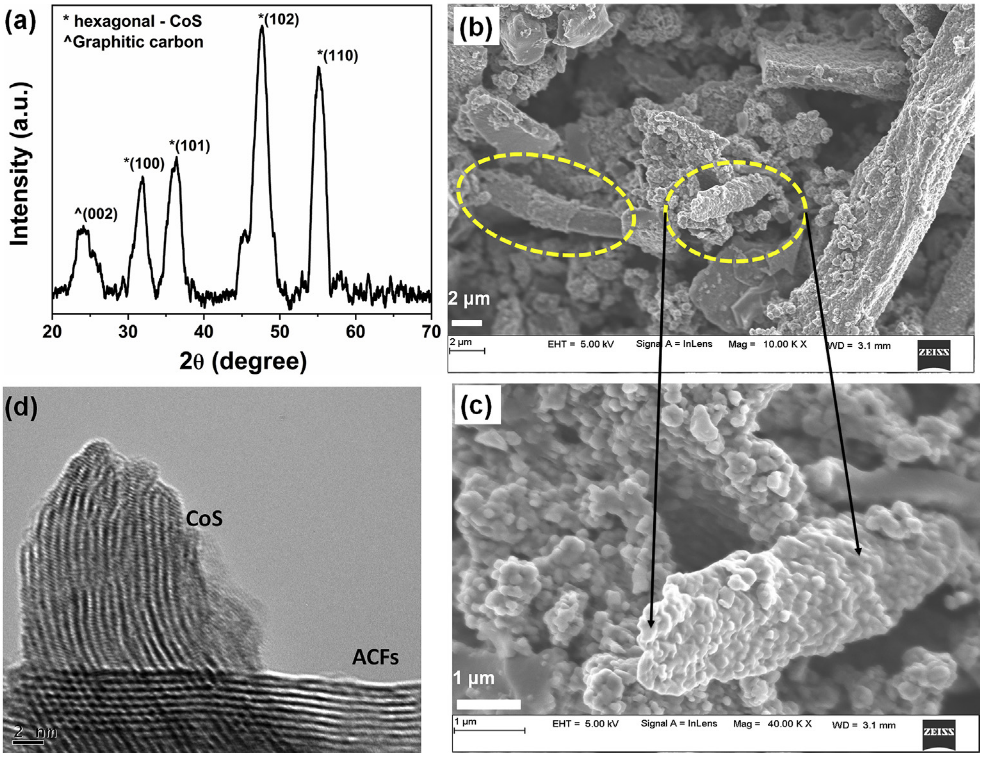

Fig. 3 – (a) XRD; (b) and (c) FESEM; (d) HRTEM of ACFs/CoS.

figure S1 and S2. It shows the presence of C and O of the CFs. While Co and S of the CoS are present in the ACFs/Composite.

Material characterization of CoS/MoS$_2$ and ACFs/CoS/MoS$_2$

The phase of MoS$_2$ and the CoS were confirmed from XRD (Fig. 4a). There are peaks corresponding to the 3-R phase of MoS$_2$ (rhombohedral phase) as well as hexagonal phase of CoS. The peaks indexed to (100), (101), (102) and (110) planes corresponds to CoS hexagonal phase (JCPDS – 65-3418). While (006), (101), (104), (009), (018) and (110) represent the 3-R phase of the MoS$_2$ [30]. There is a co-existence of 3-R phase of MoS2 and the hexagonal phases of CoS without any other diffraction peaks, which infers the purity of the phases. The

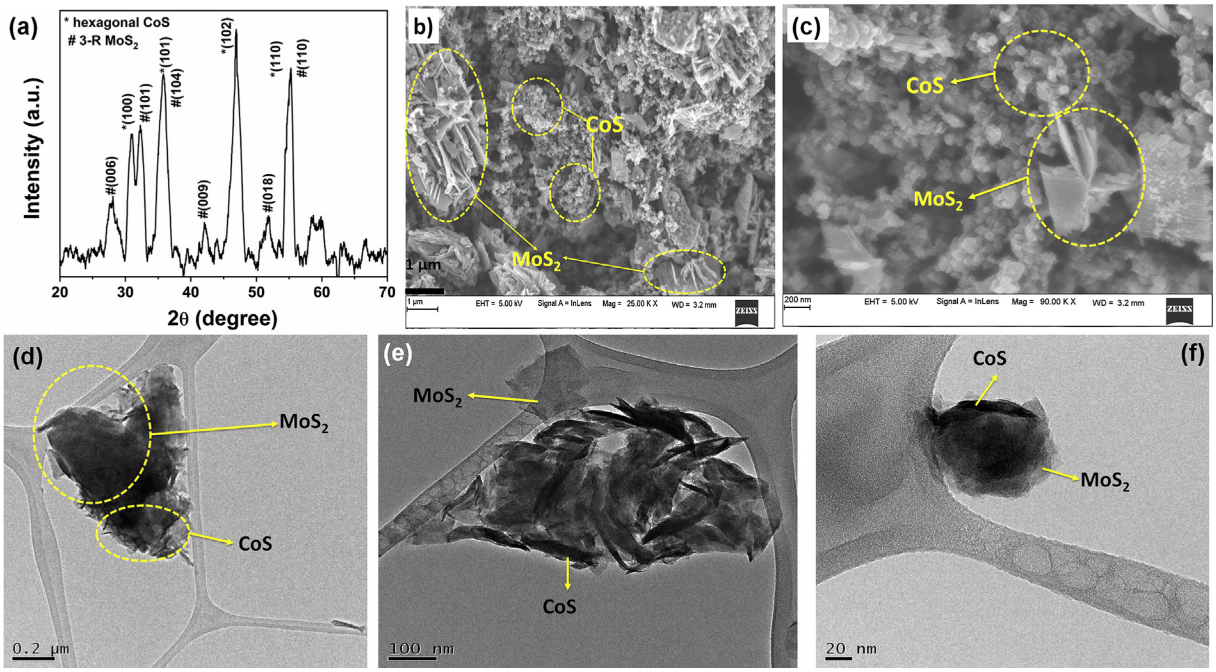

Fig. 4 – (a) XRD; (b) and (c) FESEM; (d)–(f) HRTEM of CoS/MoS$_2$.

crystallite size calculated for the FWHM of the maximum intensity peak was found to be 81 and 213 nm for CoS/MoS$_2$ and ACF/CoS/MoS$_2$ respectively. The CoS/MoS$_2$ structure indicates CoS nanosheets clubbed to appear like nodes along with the MoS$_2$ sheets. In this case, however, the sheets of CoS did not grow in any direction to form a flower morphology. But distributed randomly as marked in Fig. 4b and c. Likewise, the MoS$_2$ seems to be distributed in certain places instead of stacking like bundles together. The graphitic plane of ACFs was also found in the case of ACFs/CoS/MoS$_2$ together with the 3-R phase of MoS$_2$ and the hexagonal phase of CoS. The peak is wider, and the intensity of the (002) plane in ACFs/CoS/MoS$_2$ was found to be much lower than that of the ACFs. HR-TEM images of the CoS/MoS$_2$ composite are given in Fig. 4c, d and e. The CoS/MoS$_2$ composite if we notice, we see the edge wrinkled CoS sheets along with the plane sheets of MoS$_2$ as marked in Fig. 4c, d and e. MoS$_2$ exhibits nanosheet morphology. There is no wrapping up of MoS$_2$ sheets at any corner as observed. However, unlike in the case of CoS the flower morphology of CoS no longer exists in the case of the CoS/MoS$_2$ composite. Instead a few sheets rolled at the edges are observed. That is similar to the observation made in the FESEM images of CoS/MoS$_2$ composite. Also, these appear along with the MoS$_2$ nanosheets confirming the formation of composite. The edges of CoS appear to be wrinkled along with the plane sheets of MoS$_2$ as marked in Fig. 4c, d and e. The composite of ACFs/CoS/MoS$_2$ shows the presence of all the three components as marked in Fig. 5 c and d. Further, the inset in Fig. 5e shows the SAED pattern of the composite. Diffraction rings corresponding to (100), (101), (102) planes of CoS and (100), (110) planes of MoS$_2$ are clearly visible confirming their formation.

XPS is used to evaluate the near-surface elemental structure and the oxidation states of the detected elements in ACFs/CoS MoS$_2$. Fig. 6 shows the XPS core level spectra of the detected elements C-1s, O-1s, S-2p, Mo-3d and Co-2p. It is noticed that the primary C-1s peak is centered at 284.6 eV. Five peaks are acquired within this range while deconvoluting. The strong peak at 283.8 eV attributed to sp^2 C atom while the immediate shoulder peak to sp^3 C atoms of ACFs. The following three shoulder peaks at 285.7, 286.3 and 287.7 eV correspond to C–O–C, C–O and C═O groups. The O spectra reveals the existence of oxygen with functional groups as analyzed through C spectra. The peak at 531.1 eV indicates O–H of the adsorbed water molecules. While the other three peaks at 533.9, 532.7 and 532.1 eV features C–O–C, C–O and C═O functional groups. The additional peak at 530.7 eV indicate the existence of M–O bonds where M represents the nonmetals elements (N in the present case) [31,32]. With only traces of N being present its detection was not significant. In addition, their intensities match those depicted in the spectrum of C-1s. In case of Mo, the two characteristic peaks at 228.6 and 231.8 eV arise due to the 3d$_{5/2}$ and 3d$_{3/2}$ signals of Mo^{+4}. The Mo–S bonding is explained by the 3d$_{3/2}$ peak at 231.8 eV. S-2s is assigned at 225.8 eV. For Co, the peaks at 778.4 and 793.5 eV are attributed to 2p$_{3/2}$ and 2p$_{1/2}$ of Co^{+2} state. The binding energy separation between Co-2p$_{3/2}$ and Co-2p$_{1/2}$ is found to be 15.10 eV, which is in good agreement with the standard spin-orbit coupling of Co 2p$_{3/2}$ and 2p$_{1/2}$. Co–S bonding is characterized by a peak at 778.4 eV. No other peaks corresponding to either metallic Co or any other Co oxidation state were identified except for the shake-up satellite peak, ascertaining the purity of the CoS. The 2p spectrum of S can be fitted into four corresponding peaks. The peaks at 161.3 and 162.7 eV attributes to the S^{2-} doublets 2p$_{3/2}$ and 2p$_{1/2}$ respectively [33]. The S here exists in S^{-2} oxidation state that corresponds to both CoS and MoS$_2$. The peak at 161.3

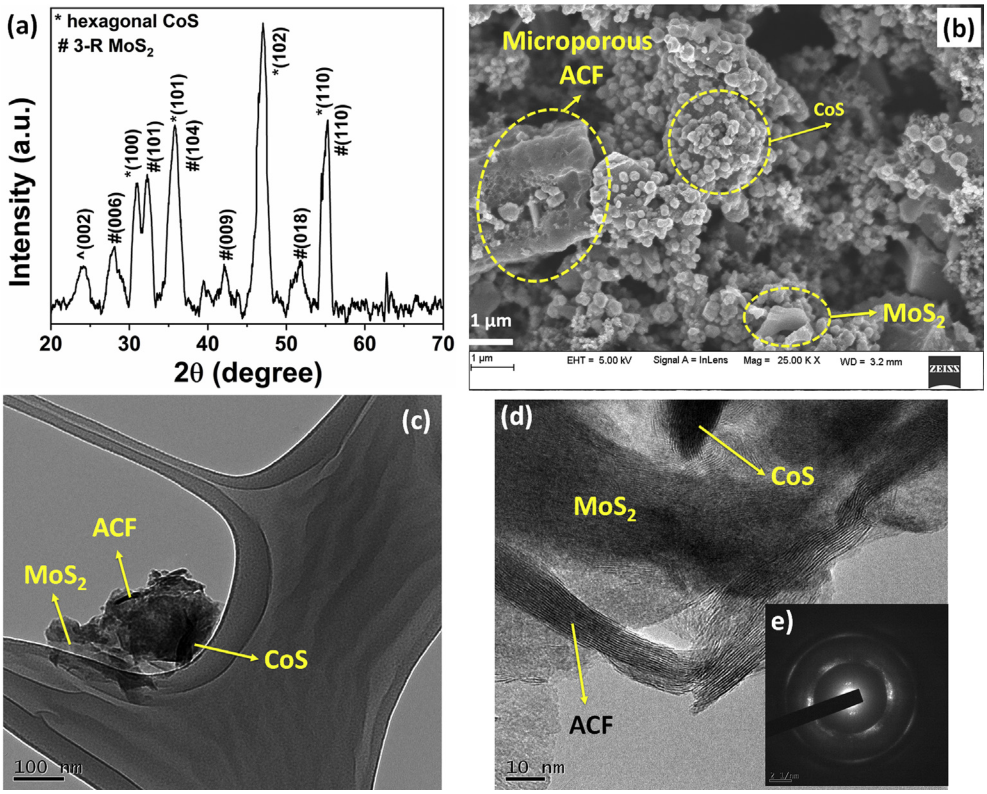

Fig. 5 – XRD; (b) and (c) FESEM; (d) HRTEM of ACFs/CoS/MoS_2.

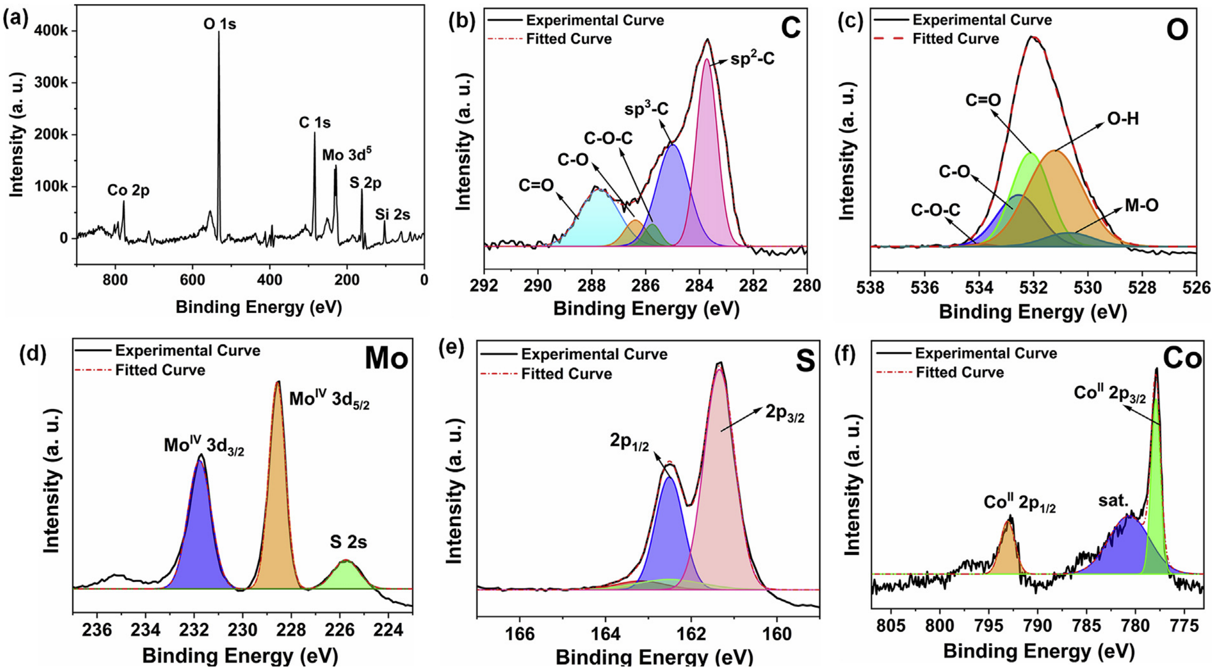

Fig. 6 – (a) XPS spectra of ACFs/CoS/MoS_2 composite, Deconvoluted high-resolution spectra of (b) C-1s, (c) O-1s, (d) Mo-3d, (e) S-2p and (f) Co-2p.

corresponding to S $2p_{3/2}$ is associated with the S of CoS and MoS_2. Small intense peaks observed at 163.2 and 162.2 eV are attributed to the presence of terminal S_2^{2-} and are believed to be beneficial for HER as they act as the catalytic sites during HER. The C–S bonding in the ACFs/CoS/MoS_2 composite can be illustrated using this peak i.e., S^{-2} of CoS and MoS_2 bonds with the C of the ACFs during the composite formation.

Supercapacitor measurements

The symmetric supercapacitor is the combination of ACFs/CoS coated on SS electrode, both as cathode and anode. HSC has anode CoS and cathode ACF/CoS coated on SS electrode. The electrochemical properties of the ACFs/CoS (Figure S5 and S6) and the ACFs/CoS/MoS_2 (Figs. 7 and 8) were analyzed. The cyclic voltammograms were recorded at various scan rates using 1 M Na_2SO_4. All the CV plots were spotted to retain similar quasi-rectangular shape over varying scan rates. However, the current response varies from the binary composite to the ternary composites. The current response for the ternary composite was found to be maximum in both (SSC and HSC) the cases as shown in Figs. 7b and 8b. There is now an additional pseudocapacitance material in the case of the ternary composite. In case of CV, this additional material contributes to the improved response. If the CV of SSC and HSC is observed, then in the case of HSC a slight change in the quasi-rectangular behavior was observed. In HSC, cathode is ACFs/CoS/MoS_2, while the anode is CoS/MoS_2. According to the plot, it would be more rational to say that the plot shape alteration is primarily due to CoS/MoS_2, where pseudocapacitance dominates the EDLC process. There is, therefore, a bump in the curve of the CV plot. The specific capacitance was calculated to be 649 Fg^{-1} for SSC and 458 Fg^{-1} for HSC at a scan rate of 2 mVs^{-1}. The specific capacitance of ternary composite SSC and HSC was three-fold higher than that of the binary composites. The specific capacitance values at 2, 5, 10, 20, 30, 50, 80 and 100 mVs^{-1} were found to be 649, 501.5, 400, 346.5, 302.1, 243.4, 195.6 and 175 Fg^{-1} for ACF/CoS/MoS_2 SSC. While for ACF/CoS/MoS_2 HSC the values are 458, 323, 250.2, 193.9, 166.4, 136.3, 111.3, 99 Fg^{-1} respectively. In the case of ACF/CoS/MoS_2 SSC, around 175 Fg^{-1} was obtained for the highest scan rate of 100 mVs^{-1}.

Studies were conducted at varying current densities to further assess the supercapacitor efficiency of the binary and ternary composite galvanostatic charge/discharge, as shown in figures S5d, S6d and 7d, 8d respectively. The typical triangular shape has been retained in all cases, except in the case of ternary composite (SSC and HSC) for slightly more IR drop. During the discharging process, the voltage initially experiences the IR drop after the current interruption. Then the voltage quickly reaches the steady state value. Now more the value of this IR drop, the time constant also will be more. The supercapacitor's response time will thus become slower. The HSC's IR drop (0.58 Ω) is greater than the SSC (0.29 Ω). 238 ms and 213 ms were reported to be their respective time constants. The higher pseudocapacitive material concentration is held primarily accountable for the much greater IR drop. The specific capacitance calculated from the GCD plot for SSC at 0.5 mAg^{-1} current density was found to be 733 Fg^{-1}. The SCs specific capacitance mainly depends on (a) adsorption/desorption of the ions at the ACFs electrode-Na_2SO_4 electrolyte interface and (b) surface faradaic reaction due to CoS/MoS_2. The higher value of the composites (ACFs/CoS and ACFs/CoS/MoS_2) specific capacitance is due to the synergetic effect of the high surface area ACFs, along with the redox behaiour of pseudocapacitance material. But, the enhanced specific capacitance of the ternary composite is mainly due to the higher percent of pseudocapacitance material's presece. When the CoS and MoS_2 are distributed on the large surface of ACFs, it provides numerous active sites for the redox reaction. That is along with the electric double layer due to the ACFs, the CoS and the MoS_2 also contributes for the redox reaction at

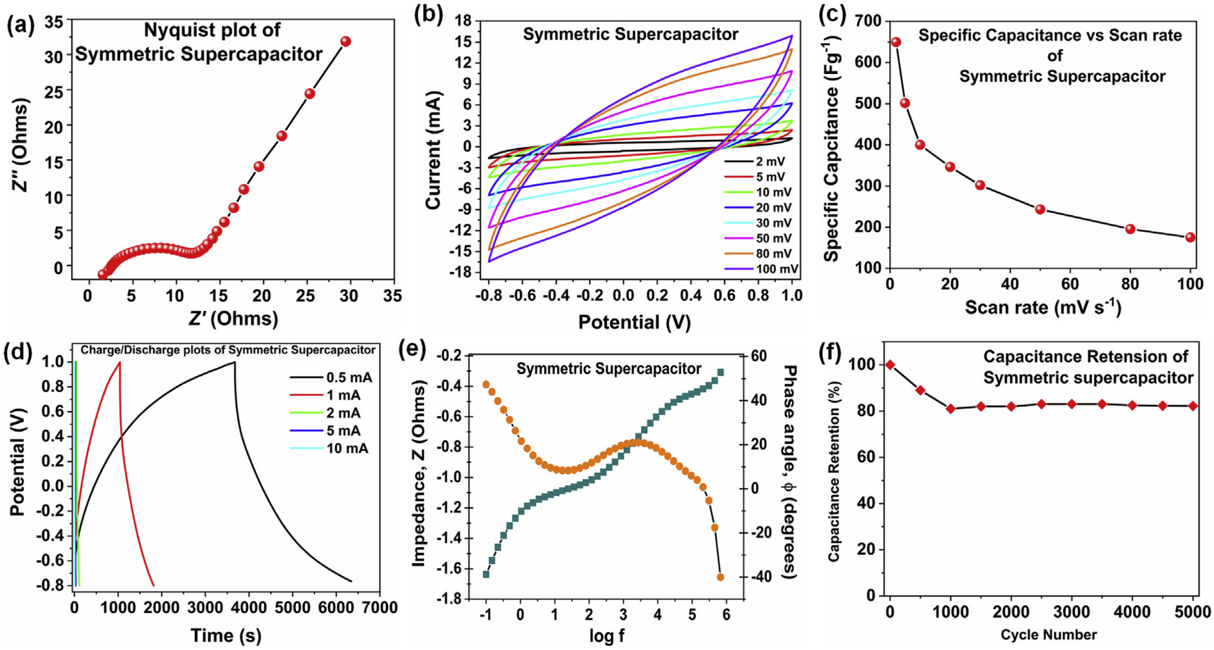

Fig. 7 – Electrochemical evaluation of ACFs/CoS/MoS_2 Symmetric Supercapacitor electrode (a) Nyquist plot; (b) Cyclic Voltammograms at different scan rates ranging from 2 to 100 mV s^{-1}; (c) Corresponding specific capacitance v/s scan rates; (d) Galvanostatic charge-discharge profiles at different current densities (mA cm^{-2}); (e) time constant plot and; (f) Cycling performance at a current density of 5 $mAcm^{-2}$ up to 5000 Cycles.

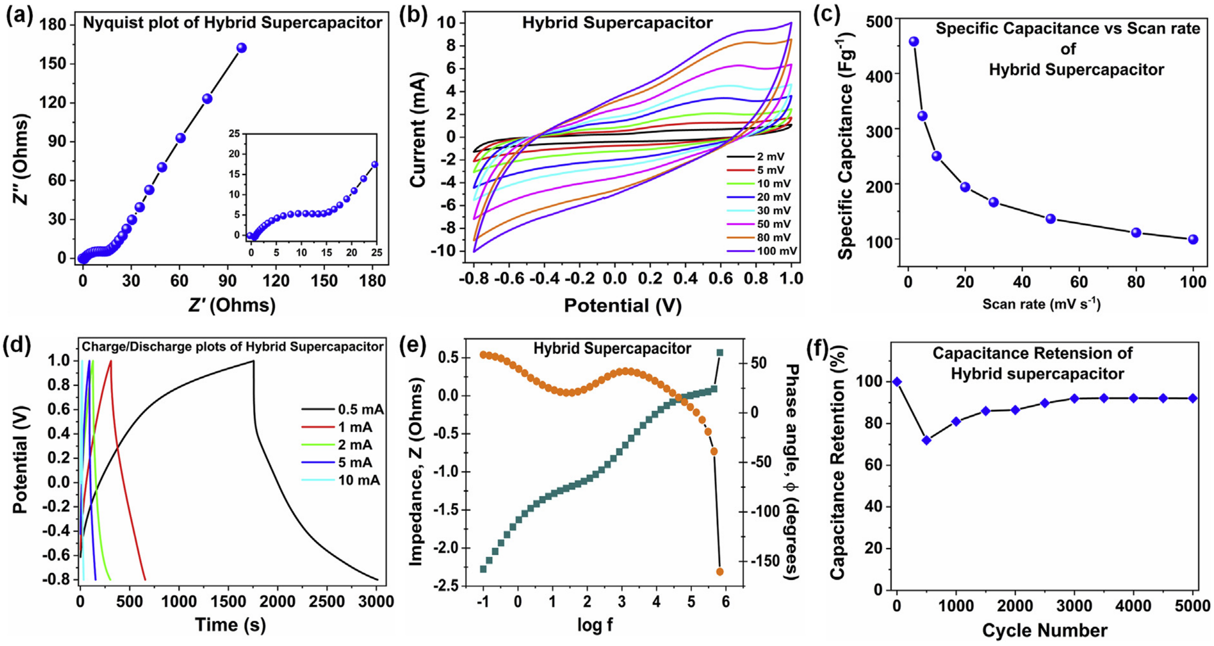

Fig. 8 – **Electrochemical evaluation of ACFs/CoS/MoS$_2$ Hybrid Supercapacitor electrode (a) Nyquist plot; (b) Cyclic Voltammograms at different scan rates ranging from 2 to 100 mV s^{-1}; (c) Corresponding specific capacitance v/s scan rates; (d) Galvanostatic charge-discharge profiles at different current densities (mA cm^{-2}); (e) time constant plot and; (f) Cycling performance at a current density of 5 mAcm^{-2} up to 5000 Cycles.**

the electrode surface. This is visible from CV, where pseudocapacitance also adds up for higher specific capacity along with the prominent EDLC behavior. The corresponding internal resistance (ESR) calculated from theIR drop of GCD plots and tabulated in Table 1. Table S1 refers to the set of values for ACFs/CoS SSC and HSC.

The EIS (Figs. 7a and 8a), on the other hand, provide a contradictory outcome for CV or GCD. The smaller the semicircle diameter, faster is the electron transfer kinetics at the electrode-electrolyte interface. However, the diameter of the semicircle was found to be lesser in case of SSC, HSC of AC/CoS binary composite. But the specific capacitance for the ACFs/CoS/MoS$_2$ ternary composite was obtained to be higher despite having a much larger EIS. The higher specific capacitance and the extended discharge time can be credited to the redox-active CoS/MoS$_2$ rather than the micropores of ACFs. The shift over the resistance and the capacitance behavior is determined using the time constant, and the plot corresponding to that is represented in figure S5e, S6e for ACFs/CoS and Figs. 7e and 8e for SSC and HSC of ACFs/CoS/MoS$_2$. The time constant for the same is calculated and tabulated in Table S1 and Table 1 respectively.

Table 1 – **Summary of the specific capacitance, equivalent series resistance, charge transfer resistance, Warburg element, energy density, power density, efficiency and time constant of symmetric and hybrid ACFs/CoS/MoS$_2$ supercapacitor.**

Type	Symmetric ACFs/CoS/MoS$_2$ Supercapacitor (SSC)	Hybrid ACFs/CoS/MoS$_2$ Supercapacitor (HSC)
Specific Capacitance from CV (Fg^{-1})	650	458
Specific Capacitance from GCD (Fg^{-1})	733	318
ESR (Ω)	0.29	0.58
R$_{Ct}$ (Ω)	10.29	14
Warburg (Z$_w$) (Ω)	15	27.5
Energy Density (WhKg^{-1})	33	15
Power Density (WKg^{-1})	999	450
N (%)	72	70
Time constant (ms.)	238	213
Stability (% retention by the end of 5000 GCD cycles)	82.2%	92.1%

The stability of a supercapacitor electrode is another significant factor. The stability of the current material was tested for over 5000 GCD cycles at 5 mAg^{-1} current density. The stability of each of the supercapacitor electrode was tabulated. Overall the ternary composite shows a better performance with higher specific capacitance, energy density, power density than the corresponding binary composite material.

HER measurements

Hydrogen Evolution reaction in an acidic medium occurs in three steps. (a) Volmer: where the proton adsorption along with the charge transfer at the electrode surface. (b) Heyrovsky: Electrochemical desorption of adsorbed hydrogen and (c) Tafel: Recombination of adsorbed hydrogen atoms to give hydrogen molecules. The corresponding theoretical Tafel slope values are 120, 40 and 30 mV respectively for each step. Hydrogen evolution reaction, however, is the combination of either Volmer-Tafel mechanism (chemical desorption of

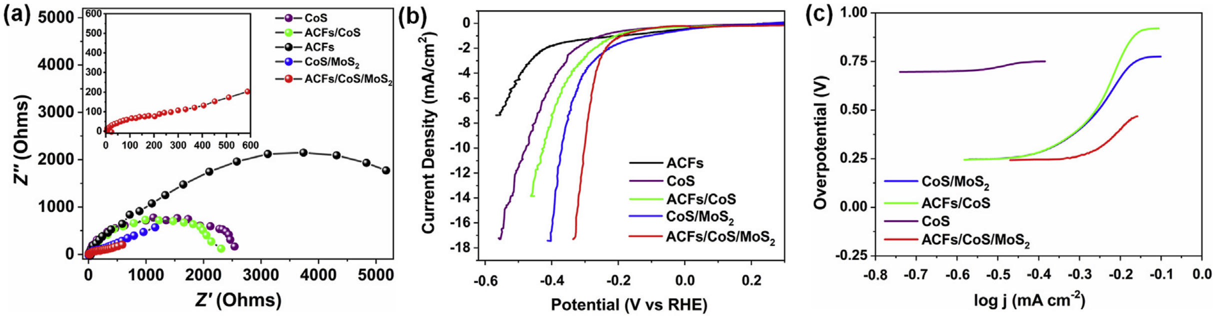

Fig. 9 – (a) Nyquist plot for of PDAC/MoS$_2$-C Composite; Electrochemical HER performance of PDAC, MoS$_2$-C, PDAC/MoS$_2$-C Composite (b) LSV and (c) Tafel plots.

hydrogen) or through Volmer-Heyrovsky mechanism (electrochemical desorption of hydrogen). Pt and Ru based compounds are highly active towards HER owing to their overpotential nearly equal to the theoretical values calculated [34]. However, their low abundance makes the need on focusing on other electrocatalysts [35]. ACFs are inactive towards HER, as shown in Fig. 9b. Electroactive catalysts CoS and MoS$_2$ are active towards HER. However, the composite displays remarkable HER by integrating CoS and MoS$_2$ on the ACFs. The evolution of hydrogen for the composites has enhanced considerably. The low conductivity of MoS$_2$ limits their catalytic performance. Coupling MoS$_2$ with a conducting surface thus could be a solution for the problem. The active sites in MoS$_2$ are the edge sites than the basal plane. On allowing to settle, the sheets of MoS$_2$ gradually stack up. This reduces the number of edge S for catalytic activity which in turn reduces the performance of the material. By ACFs as their support surface, the staking of the sheets could be minimized. The interaction of MoS$_2$ with the ACFs, led to the growth of highly dispersed MoS$_2$ nanosheets on ACFs. Similarly, if we notice CoS alone as the catalyst, we find several sheet winds together to form a flower morphology. However, when ACFs are present these sheets distribute eventually than wrapping up in certain places. This promotes more electrocatalytic sites for the HER catalysis. As we can notice in the FESEM and HRTEM images of CoS/MoS$_2$ when synthesized without a supporting surface, CoS tend to agglomerate in places and MoS$_2$ sheets stack up together. This generates a bulky catalyst

Table 2 – Comparison of the supercapacitor performance of the present work with the reported literature.

Electrode Material	Precursor for CF	Synthesis and Activation type	Specific Surface area (m^{2}g^{-1})	Specific Capacitance (Fg^{-1})	Ref.
CFs	Bamboo Chopsticks	Lignin Separation and activation/800 °C	808	–	[36]
Carbonized cotton mat	Cotton	Carbonization at 1000 °C/1 h/Ar	10	12-14 Fg^{-1} at 30 mVs^{-1} in 1 M Na$_2$SO$_4$	[11]
ACFs	Wood shavings	850 °C/180 min/Steam-N$_2$ activation	3223	280 Fg^{-1} at 0.5 Ag^{-1} in 1 M H$_2$SO$_4$	[12]
ACFs	Rayon	900 °C/1 h/Steam & 850 °C/1 h/N$_2$	3144	__	[22]
Porous Carbon Fibers	Cotton	NaOH/Urea for swelling flowed by 800 °C/2 h	584.49	221.7 at 0.3 Ag^{-1} in 3 M KOH	[37]
CF aerogel	Cotton	KOH activation/800 °C/ 90 min/N$_2$	2307	283 Fg^{-1} at 1 Ag^{-1} in 6 M KOH	[38]
Graphene fiber aerogel	Graphene oxide nanosheets	Microwave irradiation, salt addition, freeze drying, chemical reduction	477	60 Fg^{-1} at 2 mVs^{-1} in 1 M Na$_2$SO$_4$	[39]
N-functionalized CNFs	Polypropylene coated cellulose nanofibers	Electrospinning of cellulose, deacetylation and polymerization	281.8	236 Fg^{-1} at 0.2 Ag^{-1} in 6 M KOH	[40]
Silk nanofibrils	Silk	Liquid exfoliation	__	171 Fg^{-1} at 1Ag^{-1} in 1 M Na$_2$SO$_4$	[41]
Hollow carbon fibers	Catkins	Pyrolysis 800 °C/2 h/N$_2$	521.6	__	[42]
ACFs	Recycled sawdust	850 °C/1 h/Steam-N$_2$ activation	2395	242 Fg^{-1} at 1 Ag^{-1} in 6 M KOH	[43]
Porous CFs	Coal/PVA	Electrospinning	728	170 Fg^{-1} at 1 Ag^{-1} in 6 M KOH	[44]
ACFs/CoS/MoS$_2$	Banana fibres	Carbonization and KOH activation - 500 °C/1 h/ Ar	448	733 Fg^{-1} at 0.5 Ag^{-1} in 1 M Na$_2$SO$_4$	This work

structure, limiting the activity only to the electrolyte-exposed surfaces. However, such an agglomeration can be prevented when a supporting material such as ACFs is present. The ACFs 'enlarged surface area provides a platform to grow along its length for the CoS and MoS_2. Thereby avoiding the agglomeration of CoS and restacking of the MoS_2. This in turn increases the number of active sites exposed to the electrolyte. When the potential is applied, more hydrogen evolution will be achieved. The results (Fig. 9) are worth noticing that by incorporating CoS/MoS_2 in ACFs, the composite exhibit superior HER due to the increase in the active sites. In addition to that, the ACFs also provide conducting surface to further boost the catalytic activity of the composite (Fig. 9a). Furthermore, the catalytic activity of the system is enhanced when a ternary mixture is obtained. For the ACFS/CoS/MoS_2 composite, the overpotential value is much smaller than that of the ACFs/CoS composite.

Another significant indicator of the electrode material's chemical activity is the Tafel slope. The factors influencing Tafel slope values are (a) number of active sites, (b) conductivity and (c) free energy of the electrode material for HER. The Tafel slopes are shown in Fig. 9c, and their corresponding values are listed in Table 2. For the ternary composite, the Tafel slope achieved (ACFs/CoS/MoS_2) was much lesser than the other electrodes. The number of active sites for hydrogen ion adsorption and hydrogen evolution is enhanced with the distribution of CoS and MoS_2 along the length of the CFs. Thus, the ACFs/CoS/MoS_2 Tafel slope value is much smaller than the other electrodes. These values indicate a catalyst reaction comparable to that of the Volmer-Heyrovsky mechanism for hydrogen evolution, with the rate-determining step being Heyrovsky.

The Nyquist plots obtained from the electrochemical impedance spectroscopy is a useful tool to determine the electrode kinetics. Table 3 presents the values corresponding to the series resistance and charge transfer resistance. ACFs/CoS/MoS_2 showed lower series resistance and R_{CT} values among all the catalyst material, which correlates with the outcomes acquired from LSV and Tafel slopes. The ACFs/CoS/MoS_2 R_{CT} is much smaller than the other material that ensures a quicker reaction rate. 500 CV cycles were taken to verify the material performance. The material loss for the ACFs/CoS/MoS_2 is much smaller by the end of 500 cycles, of about 8% loss thus maintaining 92% of the initial ACFs/CoS MoS_2. With MoS_2 in the ACFs/CoS, the composite exhibit much better performance than the CoS/MoS_2. This is evident from the EIS. When CoS and MoS_2 nanosheets are grown on ACFs, there is well dispersion of these sheets. This in turn enhances the electrochemical active sites. Which further leads to an improved electron transfer path. The outcome from the ACFs/CoS/MoS_2 is thus an excellent HER and supercapacitance performance.

Table 3 – Summary of the onset potential, overpotential and Tafel slope values of the electrode materials.

Electrode	R_{CT}	Onset Potential (mV)	Overpotential (mV)	Tafel Slope ($mVdec^{-1}$)
ACFs	5185	−0.49	332	161.2
CoS	2562	−0.40	317	106
ACFs/CoS	2305	−0.37	314	104
CoS/MoS_2	853	−0.32	283	91
ACFs/CoS/MoS_2	245	−0.22	224	61

Conclusion

In brief, abundantly wasted banana's pseudostem fibers were efficiently transformed into conducting electrode materials. By constant variation in the amount of KOH, the surface area of the CF was enhanced from 27 to 448 m^2g^{-1} through KOH activation technique. On the prepared ACFs, the solvothermal technique was used to grow the CoS and CoS/MoS_2. Among the synthesized binary and ternary composite, the ternary composite electrodes' supercapacitor and HER activity were much higher than the other electrode materials. Thus, concluding the synergetic effect of the ACFs and the CoS/MoS_2. The ACFs ' conductive surface enhances the composites 'electrical conductivity. The growth of CoS and CoS/MoS_2 enables them to spread throughout ACFs large surface, thus avoiding stacking. Therefore, allowing a more active surface for the enhanced supercapacitor and HER performance. The current work thus encourages the synthesis of other components of multifunctional carbon materials that could be worked for better performance for numerous other applications such as batteries, Dye-sensitized solar cells, catalysis, and sensing.

Acknowledgment

The author would like to thank Manipal Academy of Higher Education for the TMA Pai Fellowship. The author also thanks the central instrumental facility of Manipal Academy of Higher Education.

Appendix A. Supplementary data

Supplementary data to this article can be found online at https://doi.org/10.1016/j.ijhydene.2019.10.033.

REFERENCES

[1] Pandolfo AG, Hollenkamp AF. Carbon properties and their role in supercapacitors. J Power Sources 2006;157:11–27. https://doi.org/10.1016/j.jpowsour.2006.02.065.

[2] Wang Q, Yan J, Fan Z. Carbon materials for high volumetric performance supercapacitors: design, progress, challenges and opportunities. Energy Environ Sci 2016;9:729–62. https://doi.org/10.1039/C5EE03109E.

[3] De Jong KP, Geus JW, Jong K, De. Carbon nanofibers: catalytic synthesis and applications. Catal Rev Sci Eng 2000;42:481–510. https://doi.org/10.1081/CR-100101954.

[4] Chung DDL. Carbon composite. 2nd ed. Elsevier Inc.; 2017. https://doi.org/10.1016/B978-0-12-804459-9/00001-4.

[5] John HA, Birnstiel ML, Jones KW. 1969 nature publishing group. Nat Publ Gr 1969;223:582–7.

[6] Hiremath N, Bhat G. High-performance carbon nanofibers and nanotubes. 2016. https://doi.org/10.1016/B978-0-08-100550-7.00004-8.

[7] Zhang L, Aboagye A, Kelkar A, Lai C, Fong H. A review: carbon nanofibers from electrospun polyacrylonitrile and their applications. J Mater Sci 2014;49:463–80. https://doi.org/10.1007/s10853-013-7705-y.

[8] Wei L, Karahan HE, Zhai S, Yuan Y, Qian Q, Goh K, et al. Microbe-derived carbon materials for electrical energy storage and conversion. J Energy Chem 2016;25:191–8. https://doi.org/10.1016/j.jechem.2015.12.001.

[9] Ding Q, Liu M, Miao YE, Huang Y, Liu T. Electrospun nickel-decorated carbon nanofiber membranes as efficient electrocatalysts for hydrogen evolution reaction. Electrochim Acta 2015;159:1–7. https://doi.org/10.1016/j.electacta.2015.01.197.

[10] Liu H-J, Wang X-M, Cui W-J, Dou Y-Q, Zhao D-Y, Xia Y-Y. Highly ordered mesoporous carbon nanofiber arrays from a crab shell biological template and its application in supercapacitors and fuel cells. J Mater Chem 2010;20:4223. https://doi.org/10.1039/b925776d.

[11] Xue J, Zhao Y, Cheng H, Hu C, Hu Y, Meng Y, et al. An all-cotton-derived, arbitrarily foldable, high-rate, electrochemical supercapacitor. Phys Chem Chem Phys 2013;15:8042. https://doi.org/10.1039/c3cp51571k.

[12] Jin Z, Yan X, Yu Y, Zhao G. Sustainable activated carbon fibers from liquefied wood with controllable porosity for high-performance supercapacitors. J Mater Chem A 2014;2:11706–15. https://doi.org/10.1039/C4TA01413H.

[13] Tao L, Zheng Y, Zhang Y, Ma H, Di M, Zheng Z. Liquefied walnut shell-derived carbon nanofibrous mats as highly efficient anode materials for lithium ion batteries. RSC Adv 2017;7:27113–20. https://doi.org/10.1039/c7ra02716h.

[14] Sowmya, Selvakumar M. Multilayered electrode materials based on polyaniline/activated carbon composites for supercapacitor applications. Int J Hydrogen Energy 2018;43:4067–80. https://doi.org/10.1016/j.ijhydene.2017.10.106.

[15] Bao SJ, Li CM, Guo CX, Qiao Y. Biomolecule-assisted synthesis of cobalt sulfide nanowires for application in supercapacitors. J Power Sources 2008;180:676–81. https://doi.org/10.1016/j.jpowsour.2008.01.085.

[16] Wang Y, Tang J, Kong B, Jia D, Wang Y, An T, et al. Freestanding 3D graphene/cobalt sulfide composites for supercapacitors and hydrogen evolution reaction. RSC Adv 2015;5:6886–91. https://doi.org/10.1039/c4ra15912h.

[17] Li N, Liu X, Li GD, Wu Y, Gao R, Zou X. Vertically grown CoS nanosheets on carbon cloth as efficient hydrogen evolution electrocatalysts. Int J Hydrogen Energy 2017;42:9914–21. https://doi.org/10.1016/j.ijhydene.2017.01.191.

[18] Sangeetha DN, Selvakumar M. Active-defective activated carbon/MoS_2 composites for supercapacitor and hydrogen evolution reactions. Appl Surf Sci 2018;453:132–40. https://doi.org/10.1016/j.apsusc.2018.05.033.

[19] Sangeetha DN, Krishna Bhat D, Selvakumar M. h-MoO_3/Activated carbon nanocomposites for electrochemical applications. Ionics 2018:1–24. https://doi.org/10.1007/s11581-018-2684-2.

[20] Thommes M, Kaneko K, Neimark AV, Olivier JP, Rodriguez-Reinoso F, Rouquerol J, et al. Physisorption of gases, with special reference to the evaluation of surface area and pore size distribution (IUPAC Technical Report). Pure Appl Chem 2015;87:1051–69. https://doi.org/10.1515/pac-2014-1117.

[21] Yoon SH, Lim S, Song Y, Ota Y, Qiao W, Tanaka A, et al. KOH activation of carbon nanofibers. Carbon N Y 2004;42:1723–9. https://doi.org/10.1016/j.carbon.2004.03.006.

[22] Gao F, Zhao DL, Li Y, Li XG. Preparation and hydrogen storage of activated rayon-based carbon fibers with high specific surface area. J Phys Chem Solids 2010;71:444–7. https://doi.org/10.1016/j.jpcs.2009.11.017.

[23] Kim CH, Kim BH. Zinc oxide/activated carbon nanofiber composites for high-performance supercapacitor electrodes. J Power Sources 2015;274:512–20. https://doi.org/10.1016/j.jpowsour.2014.10.126.

[24] Zhi M, Liu S, Hong Z, Wu N. Electrospun activated carbon nanofibers for supercapacitor electrodes. RSC Adv 2014;4:43619–23. https://doi.org/10.1039/c4ra05512h.

[25] Antunes EF, Lobo AO, Corat EJ, Trava-Airoldi VJ, Martin AA, Veríssimo C. Comparative study of first- and second-order Raman spectra of MWCNT at visible and infrared laser excitation. Carbon N Y 2006;44:2202–11. https://doi.org/10.1016/j.carbon.2006.03.003.

[26] Sagues WJ, Jain A, Brown D, Aggarwal S, Suarez A, Kollman M, et al. Are lignin-derived carbon fibers graphitic enough? Green Chem 2019. https://doi.org/10.1039/C9GC01806A.

[27] Jin J, Ding J, Klett A, Thies MC, Ogale AA. Carbon fibers derived from fractionated-solvated lignin precursors for enhanced mechanical performance. ACS Sustain Chem Eng 2018;6:14135–42. https://doi.org/10.1021/acssuschemeng.8b02697.

[28] Wang S, Zhou Z, Xiang H, Chen W, Yin E, Chang T, et al. Reinforcement of lignin-based carbon fibers with functionalized carbon nanotubes. Compos Sci Technol 2016;128:116–22. https://doi.org/10.1016/j.compscitech.2016.03.018.

[29] Schreiber M, Vivekanandhan S, Mohanty AK, Misra M. Iodine treatment of lignin-cellulose acetate electrospun fibers: enhancement of green fiber carbonization. ACS Sustain Chem Eng 2015;3:33–41. https://doi.org/10.1021/sc500481k.

[30] Ramos M, Galindo-Hernández F, Arslan I, Sanders T, Domínguez JM. Electron tomography and fractal aspects of MoS_2 and MoS_2/Co spheres. Sci Rep 2017;7:1–9. https://doi.org/10.1038/s41598-017-12029-8.

[31] Liu Z, Yu X, Yu H, Xue H, Feng L. Nanostructured $FeNi_3$ incorporated with carbon doped with multiple nonmetal elements for the oxygen evolution reaction. ChemSusChem 2018;11:2703–9. https://doi.org/10.1002/cssc.201801250.

[32] Yang L, Chen L, Yang D, Yu X, Xue H, Feng L. NiMn layered double hydroxide nanosheets/NiCo 2 O 4 nanowires with surface rich high valence state metal oxide as an efficient electrocatalyst for oxygen evolution reaction. J Power Sources 2018;392:23–32. https://doi.org/10.1016/j.jpowsour.2018.04.090.

[33] Liu Z, Yu H, Dong B, Yu X, Feng L. Electrochemical oxygen evolution reaction efficiently boosted by thermal-driving core-shell structure formation in nanostructured FeNi/S, N-doped carbon hybrid catalyst. Nanoscale 2018;10:16911–8. https://doi.org/10.1039/c8nr05587d.

[34] Wang Y, Liu Z, Liu H, Suen NT, Yu X, Feng L. Electrochemical hydrogen evolution reaction efficiently catalyzed by Ru_2P nanoparticles. ChemSusChem 2018;11:2724–9. https://doi.org/10.1002/cssc.201801103.

[35] Wang F, Yang X, Dong B, Yu X, Xue H, Feng L. A FeP powder electrocatalyst for the hydrogen evolution reaction. Electrochem Commun 2018;92:33–8. https://doi.org/10.1016/j.elecom.2018.05.020.

[36] Jiang J, Zhu J, Ai W, Fan Z, Shen X, Zou C, et al. Evolution of disposable bamboo chopsticks into uniform carbon fibers: a smart strategy to fabricate sustainable anodes for Li-ion batteries. Energy Environ Sci 2014;7:2670–9. https://doi.org/10.1039/C4EE00602J.

[37] Liu Y, Shi Z, Gao Y, An W, Cao Z, Liu J. Biomass-swelling assisted synthesis of hierarchical porous carbon fibers for

supercapacitor electrodes. ACS Appl Mater Interfaces 2016;8:28283–90. https://doi.org/10.1021/acsami.5b11558.

[38] Cheng P, Li T, Yu H, Zhi L, Liu Z, Lei Z. Biomass-derived carbon fiber aerogel as a binder-free electrode for high-rate supercapacitors. J Phys Chem C 2016;120:2079–86. https://doi.org/10.1021/acs.jpcc.5b11280.

[39] Gong C, He Y, Zhou J, Chen W, Han W, Zhang Z, et al. Synthesis on winged graphene nanofibers and their electrochemical capacitive performance. ACS Appl Mater Interfaces 2014;6:14844–50. https://doi.org/10.1021/am5016167.

[40] Cai J, Niu H, Li Z, Du Y, Cizek P, Xie Z, et al. High-performance supercapacitor electrode materials from cellulose-derived carbon nanofibers. ACS Appl Mater Interfaces 2015;7:14946–53. https://doi.org/10.1021/acsami.5b03757.

[41] Tan X, Zhao W, Mu T. Controllable exfoliation of natural silk fibers into nanofibrils by protein denaturant deep eutectic solvent: nanofibrous strategy for multifunctional membranes. Green Chem 2018;20:3625–33. https://doi.org/10.1039/c8gc01609g.

[42] Li M, Zhao Z, Liu X, Xiong Y, Han C, Zhang Y, et al. Novel bamboo leaf shaped CuO nanorod@hollow carbon fibers derived from plant biomass for efficient and nonenzymatic glucose detection. Analyst 2015;140. https://doi.org/10.1039/C5AN00675A.

[43] Huang Y, Liu Y, Zhao G, Chen JY. Sustainable activated carbon fiber from sawdust by reactivation for high-performance supercapacitors. J Mater Sci 2017;52:478–88. https://doi.org/10.1007/s10853-016-0347-0.

[44] Guo M, Guo J, Jia D, Zhao H, Sun Z, Song X, et al. Coal derived porous carbon fibers with tunable internal channels for flexible electrodes and organic matter absorption. J Mater Chem A 2015;3:21178–84. https://doi.org/10.1039/C5TA05743D.